Journal of Electroceramics (2022) 49:53–62
https://doi.org/10.1007/s10832-022-00292-9

Tuning the dielectric and energy storage properties of high entropy ceramics $(Bi_{0.2}Na_{0.2}K_{0.2}La_{0.2}Sr_{0.2})(Ti_{1-x}Sc_x)O_3$ by Sc-doping at B-site in perovskite structure

Wentao Yang[1,2] · **Guangping Zheng**[1,2]

Received: 21 February 2022 / Accepted: 17 July 2022 / Published online: 4 August 2022

Abstract

The $(Bi_{0.2}Na_{0.2}K_{0.2}La_{0.2}Sr_{0.2})(Ti_{1-x}Sc_x)O_3$ (BNKLST-*x*Sc) high entropy ceramics (HECs) have been successfully synthesized via a citrate acid method. The effects of Sc-doping on the lattice structure, microstructural morphology, dielectric and energy-storage properties of HECs are comprehensively investigated. The results indicate that although Sc^{3+} doped at B-site does not alternate the perovskite structure of BNKLST with a single phase, it results in lattice expansion and weakened bonding in TiO_6 octahedron. The dielectric constant of BNKLST-*x*Sc is reduced while the dielectric relaxation is enhanced with increasing Sc content *x*, due to the enhanced structural inhomogeneity in nano-regions. In addition, the lattice structure of BNKLST-0.2Sc exhibits ultra-high thermal stability at 30–300 °C, which achieves the maximum energy storage density of 1.094 J/cm^3 with an outstanding efficiency better than 80%, accompanying by the mechanical and dielectric losses as low as ~ 10^{-3}. It is suggested that BNKLST-0.2Sc could be promising dielectric materials in capacitors and energy-storage devices with an excellent combination of ultrahigh power density, high energy density, thermal stability as well as low mechanical and dielectric losses.

Keywords High-entropy ceramics · Dielectric capacitors · Dielectric energy storage · Dielectric properties

1 Introduction

Among lots of electrical energy storage devices, dielectric capacitors have drawn much attention because of their simple structures and device architectures, high power density, rapid charge–discharge capability, broad working temperature range and long service life [1–4]. Entropy is a thermodynamic indicator that reveals the disorder level of a material system; the configuration entropy is an important portion of system entropy which is related to the molar concentration of each constituent component in the materials, and it can be maximized in a system with equimolar principal elements. Generally, high-entropy ceramic (HEC) or oxide contains more than 4–5 principal elements in equimolar ratio. By using some advanced synthesis techniques, such as ultra-fast high-temperature sintering, the internal structure of HECs or high-entropy oxides could be stabilized [5, 6]. Particularly, HECs exhibit a generic single phase and some unique properties, such as intrinsic disorder, compositional diversity and lattice distortion, which might be conducive to enhancing the energy-storage performance [7, 8] of dielectric ceramics, especially at elevated temperatures [9]. Liu et al. [10] synthesized the $(Bi_{0.2}Na_{0.2}K_{0.2}Ba_{0.2}Ca_{0.2})TiO_3$ HECs, and found that the recoverable energy density is 0.684 J/cm^3 with an efficiency of 87.5%. In addition, Pu et al. [11] prepared the $(Na_{0.2}Bi_{0.2}Ba_{0.2}Sr_{0.2}Ca_{0.2})TiO_3$ HECs, which have a recoverable energy density of 1.02 J/cm^3 under an applied electric field of 145 kV/cm. Besides, Sun et al. [12] found that the $(Bi_{0.2}Na_{0.2}Ba_{0.2}Ca_{0.2}Sr_{0.2})$ TiO_3 HECs can achieve a recoverable energy storage density of 1.37 J/cm^3 (at 127 kV/cm). These studies show that dielectric HECs are promising for energy storage applications.

The perovskite structure (ABO_3) consists of 12-fold coordinated A cation and sixfold coordinated of B cation sublattices with octahedral oxyanions. Through tailoring

---

✉ Guangping Zheng
mmzheng@polyu.edu.hk

[1] Department of Mechanical Engineering, The Hong Kong Polytechnic University, Hung Hom, 999077 Kowloon, Hong Kong, China

[2] Foshan Xianhu Laboratory of the Advanced Energy Science and Technology Guangdong Laboratory, Foshan, China

compositions of perovskite structure at A and/or B sites, numerous interesting properties could be generated, such as catalytic [13], pyroelectric [14], piezoelectric [15], dielectric [16], ferroelectric [17], ionic-electronic conducting [18] properties. Therefore, dielectric perovskite ceramics are one of the promising candidates of energy-storage capacitors. $(Bi_{0.5}Na_{0.5})TiO_3$ (BNT), sodium bismuth titanate ceramic, exhibits large saturation polarization at room temperature ($P_s = 43$ μC/cm^2) and has high Curie temperature of 320 °C [19–21], which is considered as a key lead-free alternative to lead zirconate titanate-based materials. However, the large coercive field and high conductivity hinder its applications in dielectric capacitors. It is reported that the alternation of configuration entropy in BNT-based ceramics may offer a feasible solution in improving their dielectric and ferroelectric properties [10, 11, 22]. Meanwhile, the substitution of hetero-valent cations at B-site could result in defect dipoles in the perovskite structure [1], which affects the dielectric and energy-storage properties of materials. Wang et al. studied [23] that the P-E hysteresis loops of BNT-based ceramics became slim with the addition of $BiScO_3$ because of the transition from a ferroelectric phase to a relaxor phase. Ogihara et al. [24] reported that a high energy storage density of 6.1 J/cm^3 could be achieved in weakly coupled $BaTiO_3$-$BiScO_3$ ceramics. Luo et al. [25] have synthesized ceramics (1-x)$CaTiO_3$-x$BiScO_3$, they found that through increasing the content of $BiScO_3$, the dielectric permittivity increased and then decreased. Hence, based on our previous work on $(Bi_{0.2}Na_{0.2}K_{0.2}La_{0.2}Sr_{0.2})TiO_3$ (BNKLST) HECs [22], it is worth studying the dielectric and energy-storage properties of HECs with Sc^{3+} doped at B-site.

In this work, $(Bi_{0.2}Na_{0.2}K_{0.2}La_{0.2}Sr_{0.2})(Ti_{1-x}Sc_x)O_3$ (BNKLST-*x*Sc) were prepared by citrate acid synthesis method. Then, we systematically studied the effects of Sc-doping on the crystal structure, microstructural morphology, dielectric property, thermal stability and energy-storage property of HECs.

2 Experimental methodology

2.1 Materials preparation

We synthesized BNKLST-*x*Sc HECs with $x = 0$, 0.05, 0.1, 0.2, 0.3 and 0.5 by a citrate acid method. The raw materials of $Bi(NO_3)_3{\cdot}5H_2O$, KNO_3, $NaNO_3$, $La(NO_3)_3{\cdot}6H_2O$, $Sr(NO_3)_2$, $Sc(NO_3)_3{\cdot}H_2O$, citric acid, ammonia, tetrabutyl titanate and acetylacetone are utilized. A certain amount of citric acid, based on the stoichiometric ratio, was fully dissolved into 100 ml deionized water accompanied with ammonia to adjust the pH value to around 8. To prevent the hydrolysis reaction of Ti ions, tetrabutyl titanate and acetylacetone of volume ratio 1:1 was added to the solution. After stirring evenly at 70 °C, the separation of solution was performed to obtain the transparent titanium citrate solution. Subsequently, the above six metal nitrates were added into solution under stirring at 90 °C for several hours, following by a dehydration at 100 ˚C to generate sol and a process of yielding gel at 160 °C. The ceramic powders were obtained by calcining at 650–750 °C. The ceramic disks with Φ 8 mm and 0.5 mm in thickness and ceramic pellets with dimensions of $50 \times 7.0 \times 0.6$ mm^3 were made from a mixture of the calcined powders and polyvinyl alcohol (PVA) under a uniaxial presser at 10 MPa and 60 MPa, respectively. Finally, the samples were sintered at 1100 °C for 5 h at a heating/cooling rate of 5 °C /min.

2.2 Experimental characterization

The crystal structures of samples were characterized by X-ray diffraction (XRD, Rigaku SmartLab) equipped with Cu Kα radiation ($\lambda = 1.5406$ Å) under 45 kV and 250 mA. The micromorphology of samples was imaged by field emission scanning electron microscopy (FESEM, TESCAN MAIA3). Raman spectrometer (HR800, LabLAM) was performed at room temperature to obtain Raman spectrum under 633 nm He–Ne laser. A LCR analyzer (E4980AL, Keysight) was used to measure the dielectric properties of ceramic disks in the temperature range of -100 °C—400 °C, which were first polished and then covered with high-temperature conductive silver paste at their top and bottom surfaces. The P-E hysteresis loops and the related temperature dependent measurement were conducted by using a ferroelectric analyzer (TF2000, AixACCT). The mechanical spectra were measured on pellet samples by using a dynamic mechanical analyzer (DMA, Q800 TA Instruments) with a three-point bending testing mode.

3 Results and discussion

The XRD patterns of BNKLST-xSc HECs are revealed in Fig. 1a. Apparently, the samples ($x \leq 0.3$) exhibit a single-phase perovskite structure, indicating the Sc^{3+} ion has successfully diffused into B-site of BNKLST lattice. However, when $x = 0.5$, some secondary phases appear, such as Sc_2O_3, Ti_5O_9. The impurity phases may be caused by the difference in ionic radius between Ti^{4+} and Sc^{3+}, since the increased amount of Sc^{3+} ions could lead to the loss of coherent oxygen octahedron with Ti^{4+} and Sc^{3+} located at the center. Based on Goldschmidt tolerance factor $t = (r_o + r_A)/\sqrt{2}(r_o + r_B)$, where r_A and r_B are the average radius of ions of A- and B-sites, respectively, and r_o is the radius of oxygen [26], the stability of perovskite structure could be predicted. It is calculated that the t values of samples are 1.002 ($x = 0$), 0.998 ($x = 0.05$), 0.995 ($x = 0.1$), 0.988 ($x = 0.2$), 0.982 ($x = 0.3$)

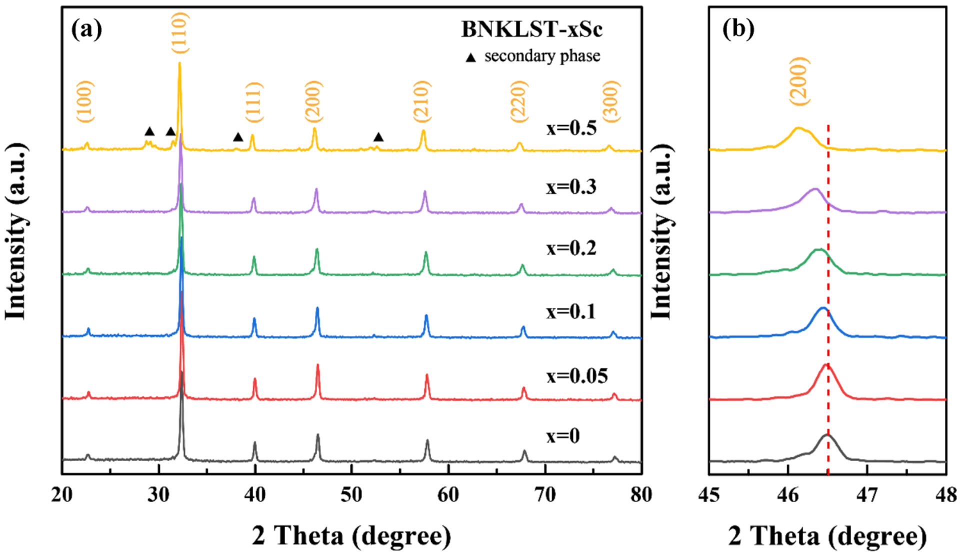

Fig. 1 XRD patterns of **a** BNKLST-xSc (x = 0, 0.05, 0.1, 0.2, 0.3, 0.5) HECs; **b** (200) peak of BNKLST-xSc HECs

and 0.968(x = 0.5). It is found that the calculated *t* values in the range of 0.97–1.03 for BNKLST-*x*Sc with $x \leq 0.3$ could indicate a single-phase perovskite structure, which are consistent with those obtained in previous studies [27]. After refinement on the XRD data for BNKLST-*x*Sc with $x \leq 0.3$, as listed in Table 1, the lattice constants *a* and *c* are found to be almost unchanged with increasing Sc content, indicating the substitution of Sc ions at B-site does not influence the crystal structure. Meanwhile, *t* decreases with increasing doping of Sc^{3+}, which also illustrates that the difference in sizes of ions at B-site may affect the formation of a single-phase perovskite structure. The ionic size difference $\delta\left(R_B\right)$ can be calculated as follows [27]:

$$\delta\left(R_B\right) = \sqrt{\sum_{i=1}^{N} n_i\left(1 - \frac{R_{Bi}}{\sum_{i=1}^{N} n_i R_{Bi}}\right)^2}, \quad (1)$$

where R_{Bi} and n_i are the radius of the i-th cation at B-site and the mole ratio of corresponding cation, respectively. With the dopant of Sc^{3+} at B-site, $\delta\left(R_B\right)$ is increased from 4.98% to 10.37%, likely leading to a lattice distortion. The influence of Sc doping on the lattice structure can be also reflected in the XRD patterns in the 2θ range of 45–48°. As shown in Fig. 1b, the (200) peak shifts gradually to a low 2θ value with increasing Sc doping, manifesting a lattice expansion according to Bragg's law [28]. Such effect of Sc doping could be ascribed to the substitution of larger ions ($R_{Sc3+} = 0.745$ Å) for the smaller ions ($R_{Ti4+} = 0.605$ Å) at B-site. Moreover, XRD patterns for BNKLST-xSc HECs at elevated temperature are measured. As shown in Fig. S1a-e, the perovskite structure is much stable up to 300 °C. Thermal expansion coefficients (CTEs) of the HECs are calculated by evaluating the lattice constant from the main (110) peak, as shown in Fig. S1f. It is found that CTE of BNKLST-xSc HECs is about $(9.08–9.81) \times 10^{-6}$ K^{-1} at 30–300 °C, which is lower than that of BNT (10.2×10^{-6} K^{-1}) [29], indicating the lattice structure of BNKLST-xSc HECs has a good thermal stability.

Figure 2a presents the Raman spectrum of BNKLST-xSc HECs at room temperature, and the active vibrational modes fitted with Gaussian profiles. The mode at a wavelength below 200 cm^{-1} is associated with A-O bonds vibrations with A being Bi, Na, K, Sr and La cations. The modes in the range of 200–400 cm^{-1} are assigned to B-O bond, and they become broader with increasing Sc concentration, indicating the increased structural disorder [30]. The band in the range of 400–700 cm^{-1}, including two main peaks (at 538 cm^{-1} and 665 cm^{-1}), are related to the vibrations of BO_6 octahedron. As shown in Fig. 2b, Raman shifts of peaks 1–3 related to A-O bonds are relatively stable with increasing Sc^{3+} content. However, the peak 6 ascribed to BO_6 shifts from 538.8 cm^{-1} (x = 0) to a lower wavenumber of 527.3 cm^{-1} (x = 0.3), demonstrating that Sc^{3+} ions are successfully doped at B-site. In addition, the full width at half maximum (FWHM) of the mode at 665.5 cm^{-1} increases from 94.8 cm^{-1} to 314.7 cm^{-1}

Table 1 Lattice constants a, c and Goldschmidt tolerance factor for BNKLST-xSc HECs

Sc content	a (nm)	c (nm)	t
x = 0	0.391	0.407	1.002
x = 0.05	0.391	0.409	0.998
x = 0.1	0.392	0.408	0.995
x = 0.2	0.392	0.408	0.988
x = 0.3	0.393	0.408	0.982
x = 0.5	0.393	0.408	0.968

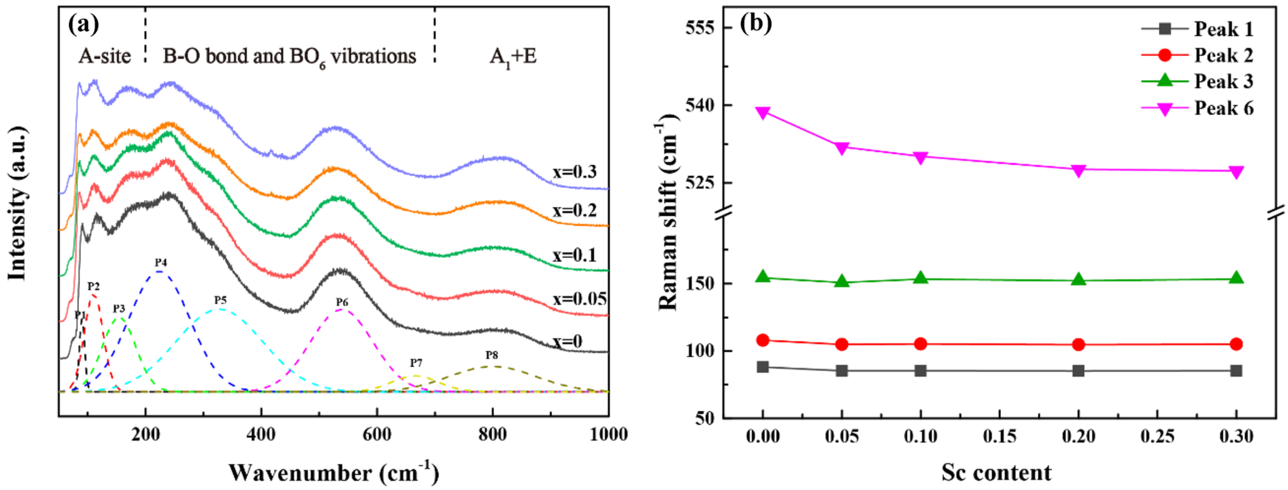

Fig. 2 **a** Raman spectrum of BNKLST-xSc (x = 0, 0.05, 0.1, 0.2, 0.3) HECs; the deconvolutions of Raman peaks 1–8 (P1-P8, from left to right) are shown as the dash curves. **b** Raman shifts of characteristic peaks versus Sc content

because of the structural expansion as caused by the substitution of Ti^{4+} with Sc^{3+}. The results thus demonstrate the introduction of Sc^{3+} at B-site could weaken the chemical bonds of TiO_6 [31], also leading to a certain degree of chemical disorder. The band over 700 cm^{-1} belongs to the A_1[LO] and E[LO] modes, which is associated with the activity of oxygen vacancies [32]. As indicated in Fig. 2a, the relative intensity of this band increases with increasing Sc^{3+} doping at B-site. It could be explained that with the increased substitution of Ti^{4+} by Sc^{3+}, more oxygen vacancies are produced to maintain the entire charge balance, and subsequently the intensity of band above 700 cm^{-1} is enhanced.

Figure 3a-e show the microstructural morphology of cross sections of BNKLST-xSc (x = 0, 0.05, 0.1, 0.2, 0.3) HECs. The grain morphologies seem to indicate that the HECs are nanostructured. The nanostructured BNKLST-xSc samples are dense as reflected by the fact that their densities measured by using Archimedes method are 96–97% relative to the theoretical densities. The nano-size grained HECs may be attributed to the high-entropy effect [22]. Because of inherent chemical disorder and lattice distortion, the diffusion of

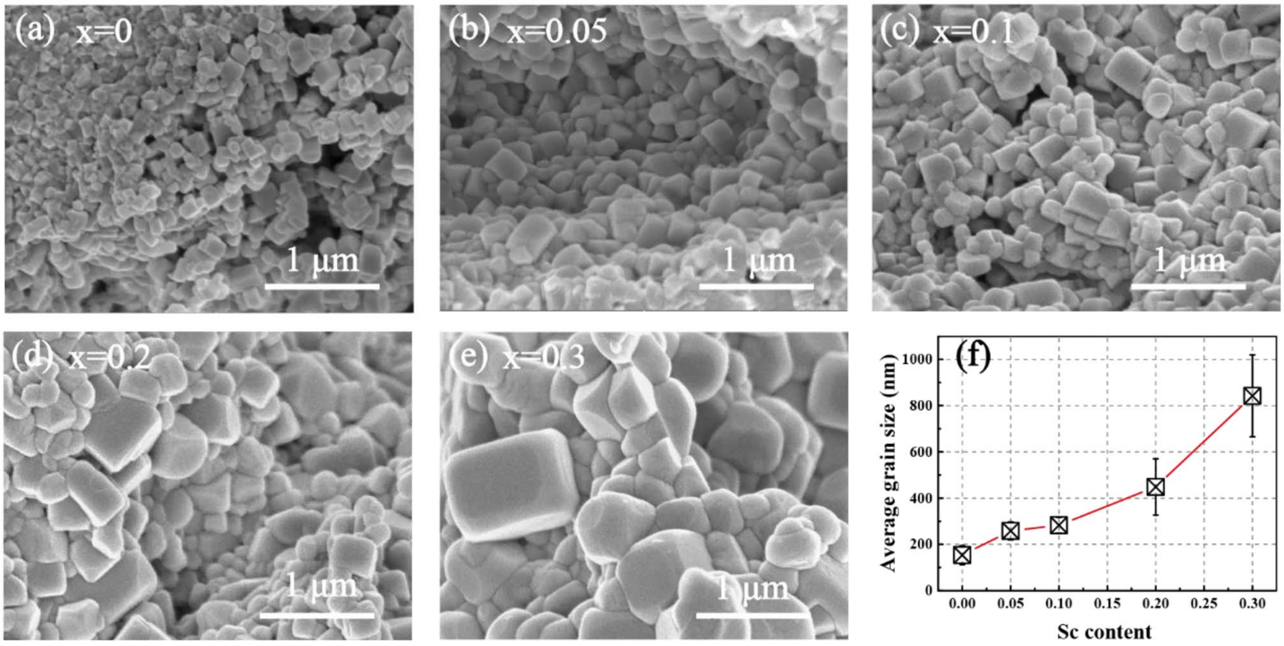

Fig. 3 **a-e** SEM images of BNKLST-xSc (x = 0, 0.05, 0.1, 0.2, 0.3) HECs; **f** The average grain size versus Sc content

atoms in the grain interior and at grain boundaries of HECs could be sluggish [33]. Consequently, the grain growth in HECs sintered at high temperatures is highly restricted, leading to nano-size grained HECs. As shown in Fig. 3f, the average grain size D increases with gradually increasing x values from $D = 153$ nm at $x = 0$ to $D = 842$ nm at x = 0.3, indicating that the increase of the Sc element can significantly enhance the grain growth in BNKLST-xSc HECs when sintered at 1100 °C. Since Sc^{3+} has a relatively larger ionic radius than that of Ti^{4+}, and it also leads to lattice expansions of perovskite structure, the diffusion of atoms in BNKLST-xSc at high sintering temperatures may be enhanced with more thermally activated vacancies related to B-sites [34]. Therefore, BNKLST-xSc has larger grain size than BNKLST. In previous studies [35, 36], it is reported that the grain sizes of dielectric ceramics have a strong effect on their breakdown electric field (E_b) and mechanical properties. Thus, the Sc^{3+} doping at B-site could be an effective approach in alternating the dielectric and energy-storage properties of BNKLST HECs.

As shown in Fig. 4a-e, the storage modulus and mechanical loss of BNKLST-xSc (x = 0, 0.05, 0.1, 0.2, 0.3) HECs are measured at the temperature ranging from 30 ˚C to 400 ˚C and various frequencies (from 0.1 Hz to 4.0 Hz). With the addition of Sc, the storage modulus (shear modulus, E) peak exhibits the trend of moving towards high temperature, and the maximum E is as high as 147–165 GPa. Due to the cocktail effect and lattice distortion in high entropy materials, the shear modulus E of HECs is found to be significantly higher than those of conventional ceramics such as BNT with $E < 100$ GPa. Meanwhile, when the content of Sc increases from 0 to 0.2, the mechanical loss of BNKLST-xSc is significantly reduced to a value lower than 0.005; especially for BNKLST-0.2Sc, the mechanical loss could be as low as 1.7×10^{-3} at the temperature above 200 ˚C. In contrast, for HECs with high Sc contents, e.g., x = 0.3, the mechanical loss is significantly increased above room temperature. The results thus indicate that appropriate Sc^{3+} doping at B-site can significantly reduce the mechanical loss of BNKLST-xSc, such as HECs with x = 0.1–0.2, which is favorable for the application of the HECs as sensors and actuators. Specifically, for BNKLST-xSc with x = 0.3, there are significant relaxation peaks of mechanical loss, which could be associated with the relaxation of oxygen in the perovskite structure. According to the Arrhenius equation $f = f_0 \bullet \exp(-E_a/k_B T_p)$, where f_0 denotes the attempt frequency, E_a represents the oxygen activation energy, k_B refers to the Boltzmann constant and T_p is the temperature of corresponding peak, E_a=1.00 eV could be calculated, which is consistent with oxygen activation energy of perovskite structures. The results further demonstrate that appropriate Sc^{3+} doping at B-site in HECs could lead to thermally stable perovskite structures with less oxygen vacancies, and consequently BNKLST-xSc HECs with x = 0.1–0.2 could have much low mechanical loss (~ 10^{-3}) at elevated temperatures.

The dielectric constants and dielectric losses of BNKLST-xSc (x = 0, 0.05, 0.1, 0.2, 0.3) HECs were measured at elevated temperature (-100–400 ˚C) with the frequency ranging from 1 kHz to 1 MHz (Fig. 5a-e). Broad dielectric peaks can be observed for BNKLST-xSc, shifting to high temperatures with increasing test frequency. Such behavior is similar with that of other ferroelectric perovskite materials [11, 37], and it may be attributed to the differences in ionic sizes and valences at B-site with the dopant of Sc^{3+}, which disrupts the long-range ferroelectric order of the structures [28]. In addition, as shown in Fig. 4, the maximum dielectric constant of BNKLST-xSc HECs decreases dramatically from 1091 at x = 0 to 233 at x = 0.3. Furthermore, to evaluate the dielectric relaxation behavior, the modified Curie–Weiss law is used to fit the data at 1 kHz, as follows:

$$1/\varepsilon - 1/\varepsilon_m = C^{-1}(T - T_m)^{\gamma}, \qquad (2)$$

where C is referred to Curie–Weiss constant, ε_m is the maximum dielectric constant occurred at the temperature T_m, and γ is a dielectric dispersion factor. Generally, γ=1 represents normal ferroelectrics, and γ=2 represents ideal relaxor ferroelectrics. As shown in Fig. 5f, with the addition of Sc element, the dielectric dispersion factor first increases and then slightly decreases. At x = 0.2, the maximum dielectric dispersion factor γ=1.68 can be obtained, which is close to that for ideal relaxor ferroelectrics. In fact, the dielectric relaxation behavior could result from the disorder of the lattice structure where the elements with different valences and ionic sizes disturb the long-range order of ferroelectrics, forming some heterogeneous nano domains and causing the dielectric dispersion behaviors. The results thus demonstrate that although there are five elements at A-site that enhance the chemical disorder, the influence of B-site doping on dielectric relaxation could be more significant, which is beneficial for the energy storage property of HECs. Moreover, the dielectric loss (tanδ) of BNKLST-xSc HECs is relatively small, especially at room temperature tanδ is found to be lower than 0.02 and the minimum (~ 10^{-3}) occurs at 30 -150 ˚C, which is favorable for dielectric application of HECs. When the temperature is higher than 150 ˚C, a sharp increase of tanδ is observed with decreasing frequency, which can be attributed to the space charge polarization in HECs [38].

The energy storage properties can be evaluated from P-E hysteresis loops, including total energy density W_t, energy storage density W_d and energy storage efficiency η, as described by the following equations:

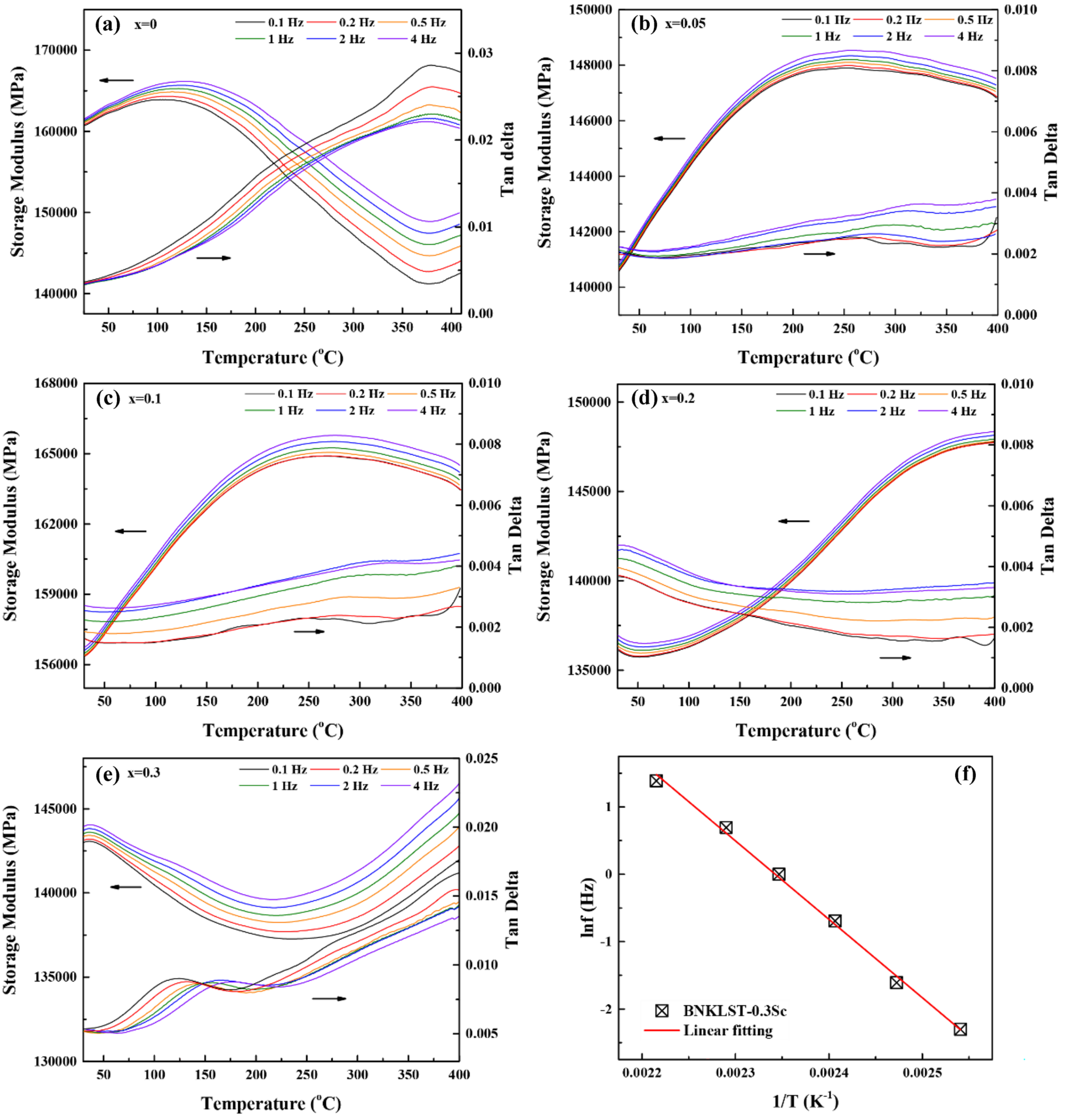

Fig. 4 **a-e** Storage modulus and mechanical loss (tanδ) of BNKLST-xSc (x = 0, 0.05, 0.1, 0.2, 0.3) HECs with various frequency at 30–400 ˚**C**; **f** The peak temperature T versus testing frequency f fitted by Arrhenius equation for BNKLST-0.3Sc HEC

$$W_t = \int_0^{P_{max}} EdP, \tag{3}$$

$$W_d = \int_{Pr}^{P_{max}} EdP, \tag{4}$$

$$\eta = \frac{W_d}{W_t} \times 100\%, \tag{5}$$

where E represents applied electric field, P_{max} and P_r refer to maximum polarization and remnant polarization, respectively. The P-E hysteresis loops of BNKLST-xSc HECs at

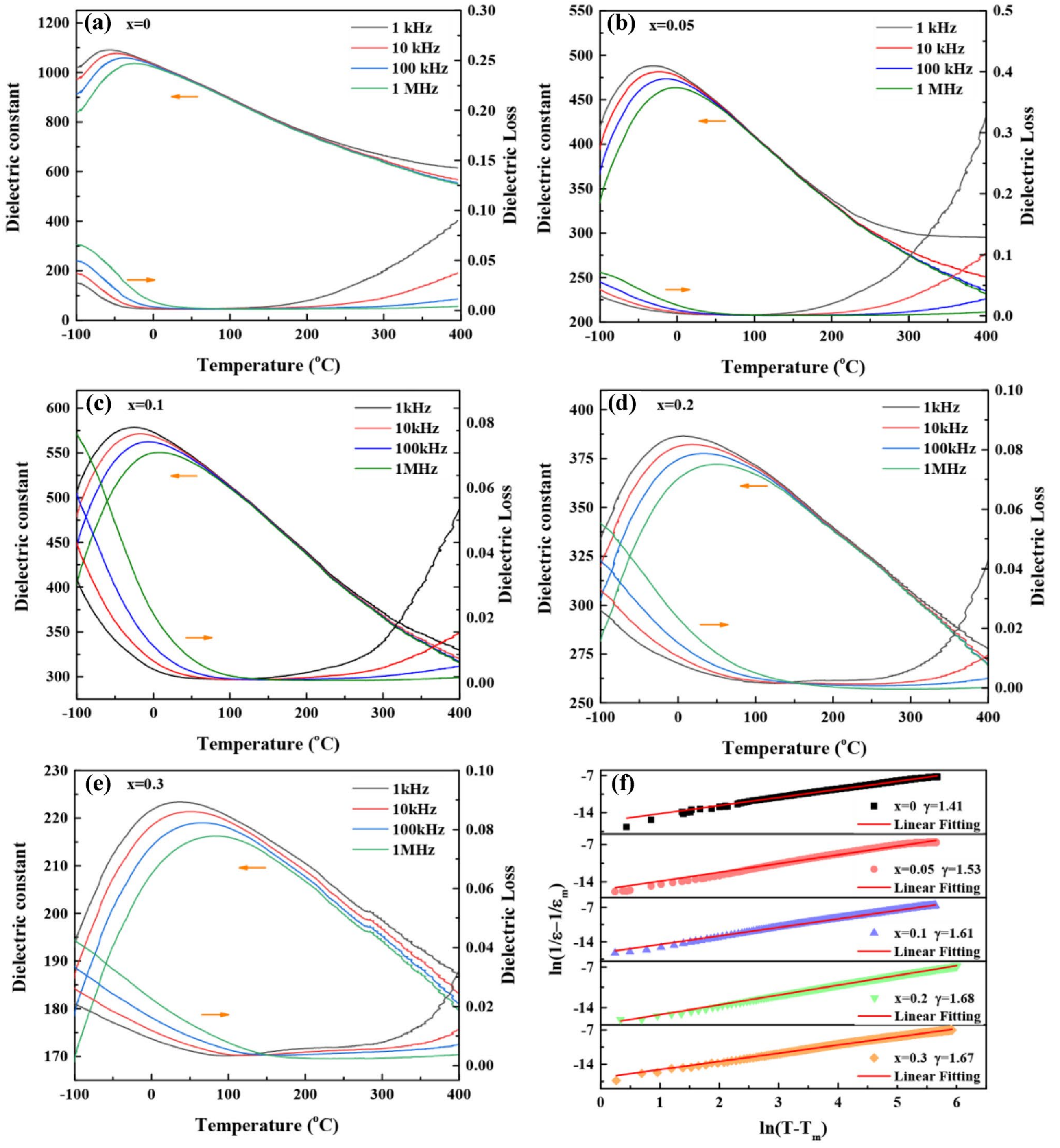

Fig. 5 **a-e** Temperature-dependent dielectric constant and dielectric loss of BNKLST-xSc ($x=0, 0.05, 0.1, 0.2, 0.3$) HECs at -100–400 ˚C; **f** The curves of $\ln\left(1/\varepsilon - 1/\varepsilon_m\right)$ vs. $\ln\left(T - T_m\right)$ and the linear fitting at 1 kHz

10 Hz are shown in Fig. 6a with the maximal applied electric field E_{max}, under which no electrical breakdown occurs during the P-E measurements; and in general the higher E_{max} the larger E_b of HECs. With Sc^{3+} doping at B-site, the P-E hysteresis loop becomes slim, while E_b dramatically decreases then increases to a maximum value of 220 kV/cm when $x=0.2$. Generally, E_b increases when there are less pores at the grain boundaries. It is found that for BNKLST-xSc HECs, when the grain size is smaller than 450 nm, appropriate increase in grain size will lead to an increase in E_b. Such phenomenon is explained as follows: in the sample with a proper increase of Sc^{3+} doping at B-site ($x=0.1$–0.2),

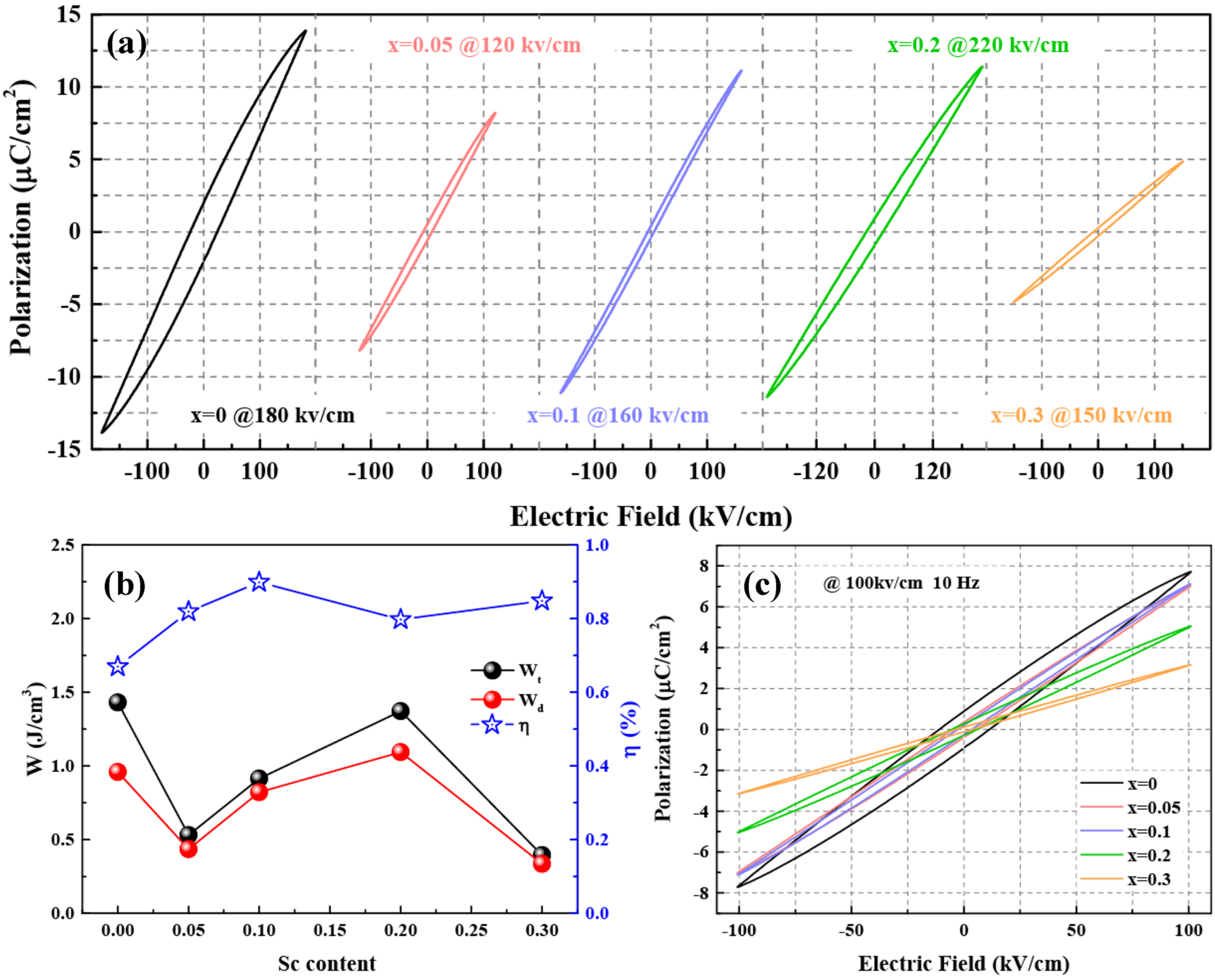

Fig. 6 **a** The P-E hysteresis loop of BNKLST-xSc (x = 0, 0.05, 0.1, 0.2, 0.3) HECs at the maximal electric fields E_{max}; **b** The corresponding total energy density, energy storage density and energy storage efficiency of BNKLST-xSc HECs vs. Sc content; **c** P-E hysteresis loop of BNKLST-xSc (x = 0, 0.05, 0.1, 0.2, 0.3) HECs at 100 kV/cm

the atomic diffusion in grain interiors and grain boundaries could be enhanced because of the lattice expansion as caused by the doping, which could facilitate the formation of smooth grain edges and corners (as shown in Fig. 3) and thereby resulting in dense grain boundaries. Consequently, BNKLST-0.2Sc could have the highest E_{max} (220 kV/cm) among the HECs studied.

As shown in Fig. 6b, BNKLST HECs have a total energy density of 1.43 J/cm^3 and energy storage density of 0.959 J/cm^3 with an efficiency of 67% under an electric field of 180 kV/cm. With the addition of 20% Sc^{3+} at B-site, a total energy density of 1.37 J/cm^3 and the maximum energy storage density of 1.094 J/cm^3 can be obtained with an efficiency of 80% under an electric field of 220 kV/cm. Figure 6c presents P-E hysteresis loops of BNKLST-xSc HECs under the same applied field of 100 kV/cm. It can be found that P_{max} decreases if the content of Sc increases, and P_r first decreases dramatically and then maintains almost unaltered until x = 0.2. This phenomenon illustrates that Sc could hinder the transformation of polar nano-regions to ferroelectric domains [39]. Besides, the P-E loops become slim owing to the increase of polar nano-regions with increasing Sc content. Since B-site doping breaks the ordered phases, some nano-regions appear in system which responds to external electric fields much faster than micro-domains, leading to a small energy loss and an enhanced energy-storage efficiency [28]. The slim hysteresis loops for BNKLST-xSc HECs indicate that they are dielectric ceramics suitable for energy storage applications.

The temperature-dependent P-E loops measurements are conducted at an applied electric field of 100 kV/cm in the temperature range of 40–200 °C. The maximum polarization,

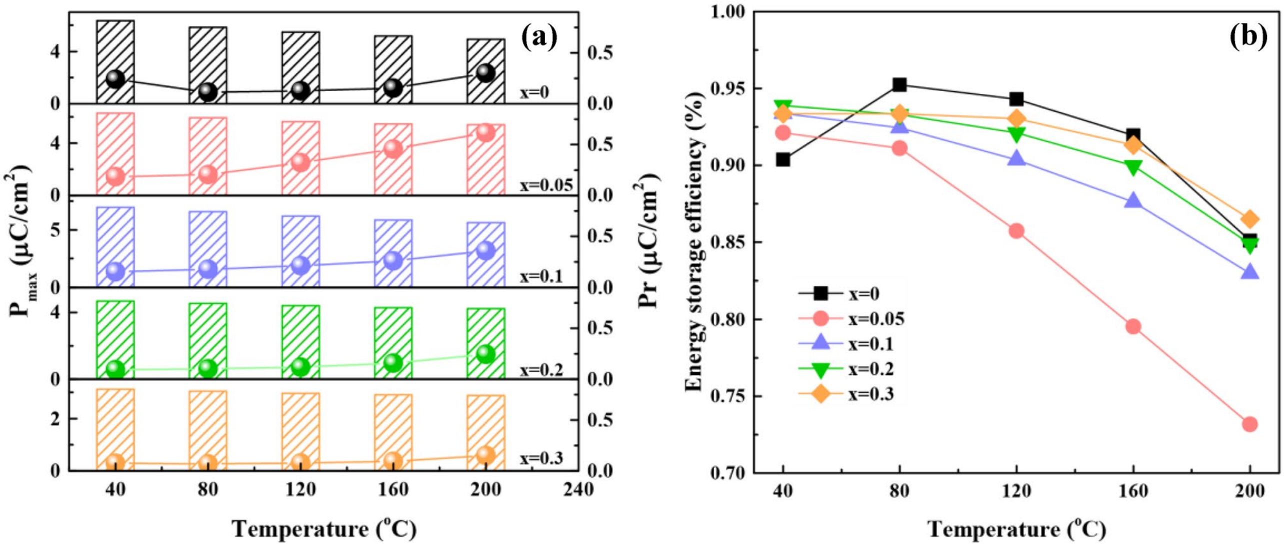

Fig. 7 **a** Temperature dependent maximum polarization (shadow bars) and remanent polarization (solid spheres and lines) of BNKLST-xSc (x = 0,0.05,0.1,0.2,0.3) HECs at 100 kV/cm; **b** Temperature dependent energy storage efficiency of BNKLST-xSc (x = 0,0.05,0.1,0.2,0.3) HECs at 100 kV/cm

remanent polarization and energy storage efficiency of BNKLST-xSc (x = 0, 0.05, 0.1, 0.2, 0.3) HECs are revealed in Fig. 7a-b. As temperature is increased, P_{max} could decrease while P_r increase for x = 0, 0.05 and 0.1. However, when $x \geq 0.2$, P_{max} and P_r maintain almost the same with an energy storage efficiency of 85%-95% at elevated temperatures, which indicate that BNKLST-xSc HECs exhibit a good thermal stability in energy storage application if the Sc content exceeds 0.1.

4 Conclusions

In summary, BNKLST-xSc HECs were synthesized via a citrate acid method. The HECs could maintain a single-phase perovskite structure when the content of Sc-doping is $x \leq 0.3$, resulting in lattice distortion and expansion. Meanwhile, the grain size of HECs increases with increasing Sc content. Raman spectrum illustrates that the introduction of Sc^{3+} at B-site weakens the chemical bonds of TiO_6, leading to chemical disorder accompanied by an increase of oxygen vacancies. As the doping content of Sc increases, the dielectric constant decreases with a dielectric loss smaller than 0.02 at room temperature, while the dielectric relaxation behavior is significantly enhanced. Among the HECs studied, at elevated temperatures of 40–200 ˚C, BNKLST-0.2Sc exhibits the maximum energy storage density of $W_d = 1.094$ J/cm^3 and has a good thermal stability with an energy storage efficiency of 85%-95%, and the related mechanical and dielectric losses could be as low as 10^{-3}. The results demonstrate that doping of Sc in HECs is an effective approach in improving their dielectric and energy storage performance.

Supplementary Information The online version contains supplementary material available at https://doi.org/10.1007/s10832-022-00292-9.

Acknowledgements This research was supported by Foshan Xianhu Laboratory of the Advanced Energy Science and Technology Guangdong Laboratory, Foshan, Guangdong Province, China.

Data availability All data generated or analysed during this study are included in this published article and its supplementary information files.

Declarations

Conflict of interest The authors have no competing interests to declare that are relevant to the content of this article.

References

1. G. Liu, J. Dong, L. Zhang, L. Yu, F. Wei, Y. Li, J. Gao, J. Hu, Y. Yan, Q. Li, K. Yu, L. Jin, Ceram. Int. **46**, 11680 (2020)
2. Z. Yao, Z. Song, H. Hao, Z. Yu, M. Cao, S. Zhang, M.T. Lanagan, H. Liu, Adv. Mater. **29**, (2017)
3. B. Chu, X. Zhou, K. Ren, B. Neese, M. Lin, Q. Wang, F. Bauer, Q.M. Zhang, Sci. (80-) **313**, 334 (2006)
4. Q. Li, K. Han, M.R. Gadinski, G. Zhang, Q. Wang, Adv. Mater. **26**, 6244 (2014)
5. L. Spiridigliozzi, G. Dell'Agli, S. Esposito, P. Rivolo, S. Grasso, V.M. Sglavo, M. Biesuz, Scr. Mater. **214**, 114655 (2022)

6. T.P. Mishra, S. Wang, C. Lenser, D. Jennings, M. Kindelmann, W. Rheinheimer, C. Broeckmann, M. Bram, O. Guillon, Acta Mater. **231**, 117918 (2022)
7. Y. Lin, N. Luo, M. Chamas, C. Hu, S. Grasso, Int. J. Appl. Ceram. Technol. **18**, 1560 (2021)
8. A. Amiri, R. Shahbazian-Yassar, J. Mater. Chem. A **9**, 782 (2021)
9. S. Zhou, Y. Pu, X. Zhang, Y. Shi, Z. Gao, Y. Feng, G. Shen, X. Wang, D. Wang, Chem. Eng. J. **427**, 131684 (2022)
10. J. Liu, K. Ren, C. Ma, H. Du, Y. Wang, Ceram. Int. **46**, 20576 (2020)
11. Y. Pu, Q. Zhang, R. Li, M. Chen, X. Du, S. Zhou, Appl. Phys. Lett. **115**, 0 (2019)
12. W. Sun, F. Zhang, X. Zhang, T. Shi, J. Li, Y. Bai, C. Wang, Z. Wang, Ceram. Int. (2022)
13. P. Tsiakaras, C. Athanasiou, G. Marnellos, M. Stoukides, J.E. Ten, Elshof, H.J.M. Bouwmeester, Appl. Catal. A Gen. **169**, 249 (1998)
14. C. Shi, L. Meidong, L. Churong, Z. Yike, J.Da Costa, Thin Solid Films **375**, 288 (2000)
15. Y. Yamashita, Y. Hosono, K. Harada, N. Ichinose, J. Japanese, Appl. Physics, Part 1 Regul. Pap Short. Notes Rev. Pap **39**, 5593 (2000)
16. X.H. Lv, W.Q. Liao, P.F. Li, Z.X. Wang, C.Y. Mao, Y. Zhang, J. Mater. Chem. C **4**, 1881 (2016)
17. T. Zheng, H. Deng, W. Zhou, X. Zhai, H. Cao, L. Yu, P. Yang, J. Chu, Ceram. Int. **42**, 6033 (2016)
18. J. Sunarso, S. Baumann, J.M. Serra, W.A. Meulenberg, S. Liu, Y.S. Lin, and J. C. Diniz da Costa. J. Memb. Sci. **320**, 13 (2008)
19. H. Wang, Q. Hu, X. Liu, Q. Zheng, N. Jiang, Y. Yang, K.W. Kwok, C. Xu, D. Lin, Ceram. Int. **45**, 23233 (2019)
20. X. Zheng, G. Zheng, Z. Lin, Z. Jiang, Ceram. Int. **39**, 1233 (2013)
21. S.K. Acharya, T.M. Kim, J.H. Hyung, B.G. Ahn, S.K. Lee, J. Alloys Compd. **586**, 549 (2014)
22. W. Yang, G. Zheng, J. Am. Ceram. Soc. **105**, 1083 (2022)
23. L. Wang, W. Bai, X. Zhao, Y. Ding, F. Wen, L. Li, W. Wu, P. Zheng, J. Zhai, J. Mater. Sci. Mater. Electron. **31**, 1491 (2020)
24. H. Ogihara, C.A. Randall, S. Trolier-Mckinstry, J. Am. Ceram. Soc. **92**, 1719 (2009)
25. B. Luo, X. Wang, E. Tian, H. Song, H. Wang, L. Li, ACS Appl. Mater. Interfaces **9**, 19963 (2017)
26. V.M. Goldschmidt, Naturwissenschaften **14**, 477 (1926)
27. S. Jiang, T. Hu, J. Gild, N. Zhou, J. Nie, M. Qin, T. Harrington, K. Vecchio, J. Luo, Scr. Mater. **142**, 116 (2018)
28. L. Zhang, X. Pu, M. Chen, S. Bai, Y. Pu, J. Eur. Ceram. Soc. **38**, 2304 (2018)
29. Y. Cao, Q. Wang, Y. Liu, X. Ning, J. Therm. Spray. Technol. **27**, 1594 (2018)
30. V.K. Veerapandiyan, S. Khosravi, H.G. Canu, A. Feteira, V. Buscaglia, K. Reichmann, M. Deluca, J. Eur. Ceram. Soc. **40**, 4684 (2020)
31. Z. Raddaoui, N. Kokanyan, M.D. Fontana, S.E. Kossi, J. Dhahri, J. Mol. Struct. **1230**, 129939 (2021)
32. R. Selvamani, G. Singh, V. Sathe, V.S. Tiwari, P.K. Gupta, J. Phys. Condens. Matter. **23**, (2011)
33. Z. Zhao, H. Xiang, F.Z. Dai, Z. Peng, Y. Zhou, J. Mater. Sci. Technol. **35**, 2647 (2019)
34. L. Wu, B. Luo, E. Tian, J. Alloys Compd. **866**, 158933 (2021)
35. Z. Yang, F. Gao, H. Du, L. Jin, L. Yan, Q. Hu, Y. Yu, S. Qu, X. Wei, Z. Xu, Y.J. Wang, Nano Energy **58**, 768 (2019)
36. J. Huang, H. Qi, Y. Gao, A. Xie, Y. Zhang, Y. Li, S. Wang, R. Zuo, Chem. Eng. J. **398**, (2020)
37. G. Dong, H. Fan, Y. Jia, H. Liu, J. Mater. Sci. Mater. Electron. **31**, 13620 (2020)
38. Y. Wu, M.J. Forbess, S. Seraji, S.J. Limmer, T.P. Chou, G. Cao, J. Appl. Phys. **89**, 5647 (2001)
39. K.T.P. Seifert, W. Jo, J. Rödel, J. Am. Ceram. Soc. **93**, 1392 (2010)